Kevlar-Covered Subresonant Pressure Sensor for Flow Measurements

Shishir Damani,* William J. Devenport,† W. Nathan Alexander,‡ and Máté Szőke§
Virginia Tech, Blacksburg, Virginia 24060
Agastya N. Balantrapu¶
University of Utah, Salt Lake City, Utah 84112
and
Timothy A. Starkey**
University of Exeter, Exeter, England EX4 4QL, United Kingdom

https://doi.org/10.2514/1.J064675

This study presents wall pressure sensors based on wall-flush Kevlar-covered cavities. The sensor dynamic response is characterized using a variety of acoustic and flow experiments, including a flow disturbance quantification performed using wall-parallel particle image velocimetry. Various sensor configurations are studied to understand the relation between cavity shape and Kevlar scrim on the sensor response. Using a localized excitation study, the sensor's spatial sensitivity is characterized, and a mathematical model to estimate the wall pressure spectrum is presented. It is shown that these sensors have a well-defined, second-order dynamic response without grazing flow. Their performance in flow shows the disturbance to the flow below the measurement uncertainty, indicating no significant flow disturbance. Comparing measured data with the model estimates reveals close agreement, within ±3 dB, and that discrepancy is accounted for by grazing flow effects and sensor spatial sensitivity.

Nomenclature

A = spatial sensitivity of a sensor
c_∞ = freestream speed of sound
f = frequency
G_{uu} = streamwise velocity spectrum
H = dynamic response function of the sensor
k_1 = streamwise angular wavenumber
k_3 = spanwise angular wavenumber
p = true wall pressure at given space and time
q = measured wall pressure at given space and time
Re_τ = friction Reynolds number
Re_θ = momentum thickness-based Reynolds number
R_{pp} = time-delay correlation of true wall pressure
R_{qq} = time-delay correlation of measured wall pressure
S_{qq} = measured wall pressure frequency spectrum
U_c = convection velocity
U_i = mean velocity component in the ith direction
U_m = maximum velocity of wall jet boundary layer
U_∞ = freestream velocity
u_i = fluctuating velocity component in the ith direction
u_τ = friction velocity
x_1 = streamwise direction
x_3 = spanwise direction
δ = boundary-layer thickness
δ^* = displacement thickness
θ = momentum thickness
τ = time delay
φ_{pp} = wavenumber–frequency wall pressure spectrum
ρ_0 = fluid density
ω = angular frequency

I. Introduction

ACOUSTIC measurements under high-Reynolds-number flows have been known to suffer from poor signal-to-noise ratios (SNRs) due to the contamination from the convective turbulent motions. Convective turbulence is a dominant contributor to the wall pressure measured by any transducer flush with a grazing flow surface. This makes it difficult to detect acoustic and nonconvective pressure fluctuations of different temporal and spatial scales. Previous studies have shown that pressure transducers with varying shapes and sizes perform spatial averaging or wavenumber filtering to measure components of the wall pressure fluctuations selectively. This implies that such measurements require correction factors to account for the averaging effect compared to wall pressure models based on point pressure relations.

White [1] performed analytical work involving transducers of different shapes and sizes. Shapes considered in this study included circular, rectangular, and diamond apertures, which were aligned in various orientations to the flow. Results indicated that the more a sensor is elongated along the flow direction, the fewer convective pressure fluctuations it detects. A circular transducer was the most sensitive to convective pressure fluctuations or flow noise. Surface sensitivity effects revealed that transducers with decreased sensitivity at their edges resolve the pressure field better than transducers with uniform sensitivity. On similar lines, Kirby [2] performed theoretical predictions of different sensor orientations and compared them with measurements on a buoyant body with differently shaped hydrophones. It was found that the transducer resolution of wall pressure is a function of the sensor area and its orientation relative to the flow. Hu [3] performed measurements and analytical work on sensor-size correction of wall pressure spectrum in various flow conditions. The effects of nonuniform sensitivity and convective scales on the correction factor were highlighted. It was only recently that cavities

Presented as Paper 2022-2956 at the 28th AIAA/CEAS Aeroacoustics 2022 Conference, Southampton, England, U.K., June 14–17, 2022; received 26 July 2024; accepted for publication 24 December 2024; published online 28 January 2025.

*Ph.D. Candidate, Kevin T. Crofton Department of Aerospace and Ocean Engineering; shishirdamani@vt.edu. Student Member AIAA.

†Crofton Professor of Engineering, Kevin T. Crofton Department of Aerospace and Ocean Engineering. Fellow AIAA.

‡Associate Professor, Kevin T. Crofton Department of Aerospace and Ocean Engineering. Associate Fellow AIAA.

§Senior Research Associate, Kevin T. Crofton Department of Aerospace and Ocean Engineering. Member AIAA.

¶Assistant Professor, Department of Mechanical Engineering. Member AIAA.

**Senior Research Fellow, Centre for Metamaterial Research and Innovation.

with embedded microphones at their base were employed to study turbulent boundary-layer wall pressure. VanDercreek et al. [4] studied 12 different cavity geometries defined by their depth, chamfer, diameter, opening ratio, and mesh covering to quantify the effects of these parameters on the spectral energy and SNR. It was shown that the observed spectral energy reduced exponentially with an increase in the cavity depth. Mesh coverings improved the SNR by 5 dB, and reduction in cavity area with depth also improved the SNR. D'Elia et al. [5] studied Kevlar-covered Helmholtz resonators in the hope of suppressing flow effects and allowing acoustics to pass through; however, the authors revealed a transmission loss associated with Kevlar that needs to be accounted for.

From a recent study in the field of acoustic metamaterials, Damani et al. [6] demonstrated the generation of acoustic surface waves on the nonflow side of a metasurface excited by turbulent pressure fluctuations on the flow side, the two being connected through a half-wave resonator that supported standing waves corresponding to wavelengths of $n\lambda/2$. The study used a periodic arrangement of 18 mm slots with their major axis perpendicular to the flow, and all but one of the slots were quarter-wave resonators ($(2n-1)\lambda/4$ modes) 21.5 mm deep and open only to the underside of the metasurface. The one exception was a single 43-mm-deep half-wave resonator, nominally open at both ends, that connected the underside to the flow surface and the pressure fluctuations generated by the overriding turbulent wall jet. The top end of this resonator was covered by a thin (0.08 mm) Kevlar 120 scrim, as used in hybrid anechoic wind tunnels, because of its transparency to pressure fluctuations and its near-impervious nature to flow, provided that there is no significant dynamic pressure difference between the two sides. The depths of the half-wave and quarter-wave resonators implied a fundamental resonant frequency close to 4 kHz. The spanwise dimension of the slots (17 mm) did not permit spanwise acoustic modes at frequencies below about 10 kHz.

The study by Damani et al. [6] motivates this present work because the resonator cavity used to connect the flow with the metasurface suggested a novel measurement strategy for filtering convective pressure fluctuations to measure subconvective and acoustic/supersonic components across the surface. Specifically, if one imagines placing a point pressure transducer at the bottom of the through cavity, then such a transducer would measure a signal proportional to the area-averaged pressure exerted by the flow on the Kevlar-covered spanwise slot in the flow at the top surface of the cavity. An important presumption here is that the pressure field in the cavity responds in a coherent, spanwise uniform fashion to the largely incoherent nonuniform excitation imposed by the overriding boundary layer, and indeed, this was shown to be the case for frequencies below the spanwise acoustic mode. Following this, a concept for an evolved sensor can be put forward.

Transforming the half-wave resonator into a quarter-wave resonator enables the use of an off-the-shelf pressure transducer to be installed at the base of the cavity. Replacing one open end of the cavity with a closed end removes a source of contamination, which was the case with the half-wave resonator with two open ends. Assuming the same depth for a half-wave and a quarter-wave cavity, the fundamental acoustic resonance of the quarter-wave cavity halves compared to a half-wave cavity. Figure 1 shows a schematic of the resonator-based sensor, with Fig. 1a showing the acoustic resonant cavity and Fig. 1b a Kevlar scrim covering the cavity underneath. Note that the sensing element is a microphone, but the entire assembly of the acoustic cavity, Kevlar, and the microphone constitutes the sensor. A Kevlar scrim allows transparency to pressure fluctuations on the surface and prevents any measurable flow disruptions. The volumetric acoustic cavity is defined by its shape (rectangle in the schematic) and depth. These sensors are easy to construct using rapid prototyping technology and inexpensive electret microphones. An array of such sensors was used by Damani et al. [7] to measure subconvective pressure fluctuations in zero-pressure gradient turbulent boundary-layer flows. The cavity length was chosen to be on the order of the boundary-layer thickness to spatially filter flow-relevant convective pressure fluctuations.

This present study investigates dynamic sensor responses to explore the assumptions and possibility of employing such sensors for acoustic testing in the presence of flow. Furthermore, a mathematical model to estimate the wall pressure spectrum from such sensors is described based on some assumptions to tailor their design based on the purpose. Section II details the type of cavities tested and the corresponding methods and experimental setups used to examine various aspects of the sensor. This is followed by presenting a mathematical model to estimate the wall pressure spectrum using such sensors in Sec. III. The results are addressed by the coherence of the pressure field at the base of the cavity, understanding the effects of cavity shapes on the dynamic response of the sensor, investigating the spatial sensitivity over the surface, and quantifying any effects of the Kevlar scrim on the overlying flow excitation in Sec. IV. We found that Kevlar-covered resonant sensors have minimal influence on an overriding flow, exhibit an almost uniform spatial sensitivity distribution, and can take on any profile shape; however, their response is limited by the first mode along their length. The proposed sensors appear useful in designing arrays with new capabilities such as measuring acoustic signals through boundary layers.

II. Scope of Measurements

Acoustic and flow measurements were performed on different Kevlar-covered resonator-based sensors to evaluate their dynamic response and interference with flow. A series of nine sensor configurations comprising different profile shapes and Kevlar grades were studied. The sensors are quarter-wave resonating cavities manufactured using stereolithography (SLA) rapid prototyping technology. The 3D printing was conducted on the Connex 3 printer with Acrylonitrile Butadiene Styrene (ABS) Plus plastic. The printer produced smooth profiles with a layer thickness of 16 μm.

A list of the sensor configurations tested is shown in Table 1, with open area ratio (OAR) defined as the ratio of the effective open area to the total surface area of the shape. The OAR was evaluated as the area of open pores between Kevlar weaves over a defined area using microscopic images of the Kevlar scrim. The slot shape is considered as the benchmark case, derived from the study by Damani et al. [6]. The slotted profile comprises a rectangle 15 mm in length capped by a semicircle 1.5 mm in radius on either side. The Hanning profile refers to a Hanning window shape mirrored about the base with a maximum

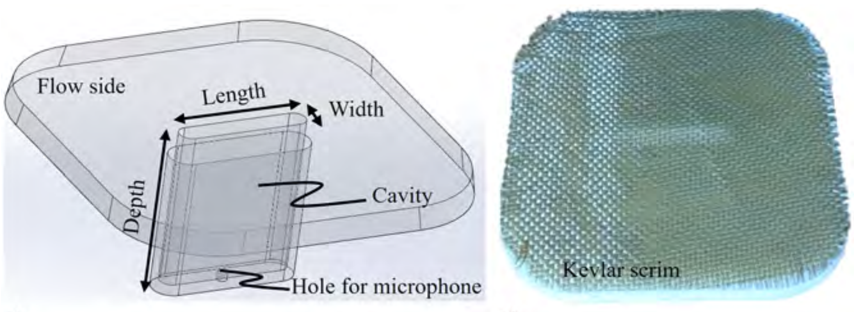

Fig. 1 a) CAD view showing the cavity and the location of the microphone. b) Flow side of the cavity with Kevlar scrim as manufactured. Note: the flow direction can be parallel or perpendicular to the length dimension.

Table 1 Different sensor configurations studied

Sensor	Profile	Dimensions in mm	Kevlar Type (thickness)	OAR, %
A	Slot	18/3/21	None	100
B	Slot	18/3/21	Kevlar 120 (0.08)	2
C	Rectangle	18/3/21	Kevlar 120 (0.08)	2
D	Rectangle	50/3/21	Kevlar 120 (0.08)	2
E	Hanning	18/3/21	Kevlar 120 (0.08)	2
F	Slot	18/3/42	Kevlar 120 (0.08)	2
G	Slot	18/3/21	Kevlar 49 (0.14)	0.01
H	Slot	18/3/21	Kevlar (0.08)	6
J	Rectangle	50/3/30	Kevlar 120 (0.08)	2

The dimensions specify the length, width, and depth, respectively, as seen in Fig. 1.

window height of half the cavity width. A minimum wall thickness of 5 mm was chosen to print these cavities to suppress any significant coupling with the structural modes of the material. Each printed cavity was part of an insert mounted onto a 609.6 mm × 609.6 mm, 4.76-mm-thick aluminum plate such that the insert was flush on one side of the plate.

Measurements were performed in the Virginia Tech Anechoic Wall Jet Facility as described in Sec. II.A. The insert was secured to the plate using a 40-micron tape applied to the perimeter of the insert, ensuring minimum diffraction and disturbance to flow. The Kevlar scrim was applied over the cavity using spray adhesive (3M Hi-Strength 90), ensuring that no residue stayed on the excited surface. Some reference measurements were performed without a Kevlar scrim. A probe tip microphone (Brüel & Kjær Type 4182) with a 25-mm-length tip was utilized to measure the pressure fluctuations flush with the base of the cavity with no pressure leakage.

A. Anechoic Wall Jet Facility

This study was performed in the Virginia Tech Anechoic Wall Jet Tunnel. A schematic of the facility is shown in Fig. 2, including an acoustically treated settling chamber, contraction chamber, nozzle exit, and a flat test plate housed in an anechoic chamber. The tunnel intakes air via an airbox equipped with a steel discharge silencer and passes it on to an acoustically treated settling chamber via a flexible hose. This flexible hose mechanically isolates the blower from the rest of the tunnel. After the settling chamber, the flow passes through a contraction and out over a large plate 3048 mm long, 1524 mm wide, and 9.525 mm thick via a nozzle 12.7 mm tall and 1219 mm wide. Further description of the settling chamber and contraction is given in the work of Kleinfelter et al. [8]. The plate is made of Aluminum 6061-T651 and sits in an anechoic chamber. The bottom surface of the test plate is 1333.5 mm above the ground, supported by a three-piece steel frame. The anechoic chamber is 4.718 m long, 3.238 m wide, and 2.744 m tall, made with an aluminum skeleton lined with medium density fibreboards (MDF) boards for sound insulation. The inside of the anechoic chamber is covered with 101.6 mm acoustic wedge foam and 152.4 mm square bass corner foam. The end of the test plate has a curved edge to promote the Coanda effect to deflect the flow gradually. The tunnel can achieve a maximum flow speed of 70 $\mathrm{m \cdot s^{-1}}$ at the nozzle exit. The tunnel produced a fully turbulent flow over the surface of the plate. The test area comprising the large aluminum plate had a 609.6 mm × 609.6 mm provision for custom instrumentation panels. The edge location of the provision was 1130 mm away from the nozzle exit. The wall-jet tunnel nozzle exit speed was calculated by converting the pressure drop between the settling chamber and the jet exit. The pressure drop was measured using a water column manometer, giving a tunnel speed accuracy of 0.1 m/s. Additionally, temperature was also recorded at the nozzle exit location to determine the properties of air.

B. Sensor Dynamic Response Testing

The dynamic response of the sensor was measured using a conventional acoustic calibration procedure. The dynamic response refers to the transfer function between the pressure field at the Kevlar scrim and the pressure field at the base of the cavity. The experimental setup involved an acoustic source (Visaton FRS8-8 Ohm speaker) 76.2 cm away from the surface such that the speaker center was aligned with the center of the cavity, as shown in Fig. 3.

Using cross-correlation analysis on the measured pressure signal by the microphone at the base of the sensor and a reference measurement made at the surface of the Kevlar scrim with the input signal to the speaker yields the transfer function given by

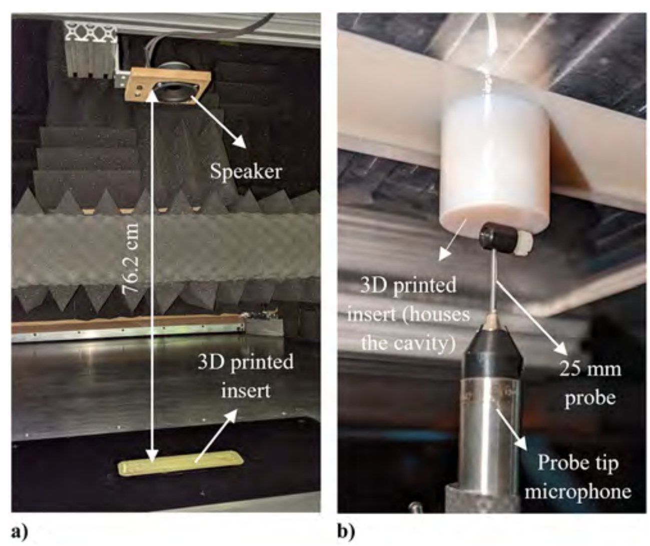

Fig. 3 Setup for measuring the dynamic response of a sensor in the wall jet facility: a) excitation side; b) cavity side.

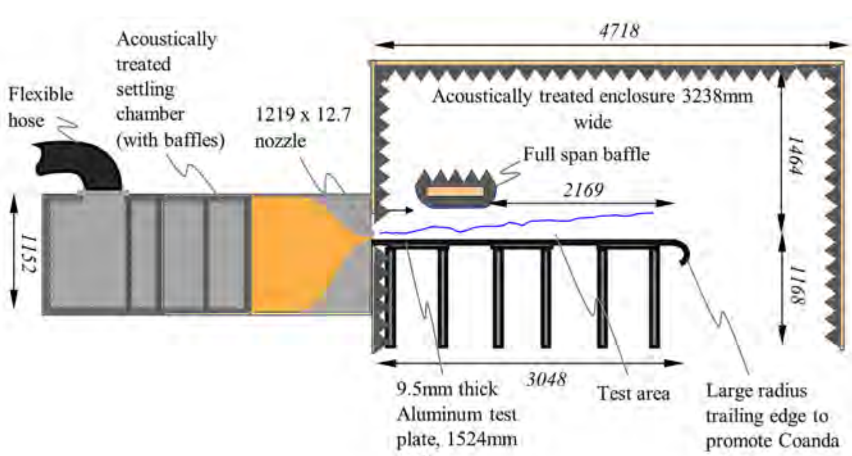

Fig. 2 Schematic of Virginia Tech Wall Jet Wind Tunnel. All dimensions in mm.

$$H(\omega) = \frac{G^c_{mw}}{G^c_{ww}} \times \frac{G^s_{ww}}{G^s_{mw}} \quad (1)$$

where G_{mw} is the cross-spectrum between the microphone and the white noise signal, G_{ww} is the autospectrum between the white noise, and the superscripts s and c represent the two measurement configurations referred to as the surface and the cavity. The surface configuration was a wall pressure measurement with the microphone flush with the surface with no Kevlar. The sensor configuration included the cavity and the microphone at its base. Data were obtained for 32 s with a sampling rate of 65,536 Hz. The spectrum evaluation used Welch's method with a record size of 8192 samples and 50% overlap, giving a total of 511 averages.

C. Sensor Spatial Sensitivity Measurement

The pressure field inside the cavity was quantified using two probe microphones (Brüel & Kjær Type 4182). One microphone was fixed at the center of the base, while the other was moved to discrete locations along the length of the cavity, as shown in Fig. 4. The stationary microphone was introduced from the side of the cavity at the base, as there was insufficient room to accommodate both microphones at the bottom face. Sensor types B and E from Table 1 were tested with five and four discrete locations along the cavity. The locations were chosen based on working space and the microphone size. Measurements were conducted with the wall jet boundary-layer flow as the excitation source. The boundary-layer properties above the sensor were $\delta = 13.3$ mm (boundary-layer thickness) and $U_m = 24\ \mathrm{m \cdot s^{-1}}$ (maximum local velocity). The uniformity was studied using the coherence and phase relations between the two microphones at the sensor bed.

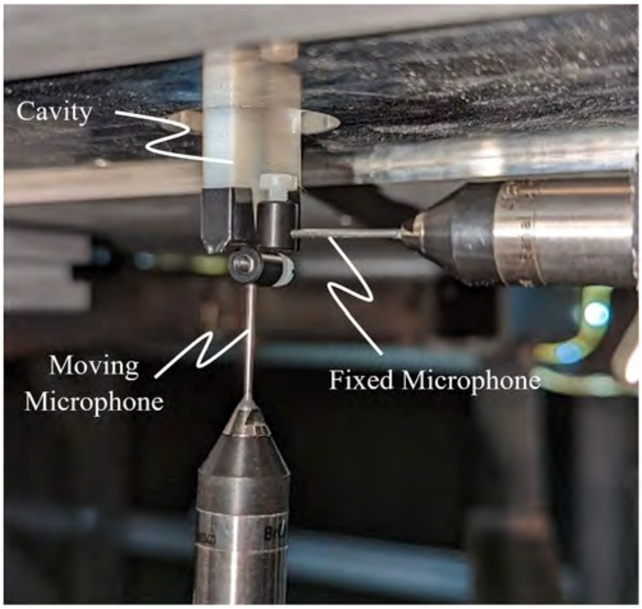

Fig. 4 Schematic of coherence testing at the base of the sensor.

In addition to the pressure field at the base of the cavity, it is important to quantify the sensor response over the Kevlar scrim, i.e., spatial sensitivity. An acoustic experiment was designed to quantify this behavior; this utilized a localized sound source with a monopole character in the range of frequency of interest. A KOSS sparkplug earphone (operating frequency range of 16–20,000 Hz) was chosen for this purpose. The earphone was mounted on a low-profile rod supported on the existing structure in the wall jet facility.

The monopole characteristic was evaluated using measurements that showed a uniform directivity and an amplitude scaling as $1/r$ within ± 3 dB, where r is the radial distance between the source and the measurement point. The spatial sensitivity of the sensor was assessed by analyzing the sound field using sensor type D detailed in Table 1. The sensor, measuring 50 mm in length, 3 mm in width, and 21 mm in depth, was designed to resonate at 3.4 kHz in span mode and 4 kHz in depth mode, excluding any effects of the Kevlar interface. The measurement procedure mirrored that of the dynamic response measurement for the sensor, with the source traversing over the sensor at a consistent height h of 2 mm above its surface. Seven distinct locations were selected across the sensor area, with five directly over its profile and two extending beyond its dimensions (one on each side). The setup with a near-field source is depicted in Fig. 5a, featuring the source positioned over a flush-mounted surface microphone for reference measurements. Figure 5b displays a photograph of the source atop the Kevlar-covered sensor. For each source excitation location, data were acquired by a probe microphone at the center of the quarter-wave cavity bed. The spatial sensitivity was studied using the sensor's dynamic response that captured the degree of spatial averaging influenced by different source positions. A uniform spatial sensitivity would manifest as no alterations in the dynamic response function.

D. Wall-Parallel 2-Dimensional, 2-Component (2D2C) PIV

The flow over the cavity opening was imaged using a two-dimensional high-speed particle image velocimetry (PIV) system to assess any potential interaction between the flow and the cavity. Flow interference measurements were made using sensor F in Table 1, which is a 42-mm-deep half-wave cavity (open lower end) with a slot-shaped profile 18 mm by 3 mm, covered with 2% OAR Kevlar 120 scrim.

This configuration is a more stringent test, considering that the open-open cavity may impact the boundary-layer flow more significantly than a cavity closed at the bottom. The cavity was placed with its long axis spanwise across the flow. The Kevlar covering formed a rectangular patch that extended ± 25.4 mm from the center of the cavity in spanwise and streamwise directions. To examine this in detail we consider a wall-parallel cross section of the flow located 1.25 mm from the surface and measured using planar PIV. The region of study is 75 mm in the flow direction (x_1) and 46.5 mm across the flow direction (x_3). Measurements were made of the flow over the Kevlar-covered cavity and the flow over a plain wall (with no cavity). The entire Kevlar-interfaced cavity was part of the flowfield, and its location is highlighted in the results discussed.

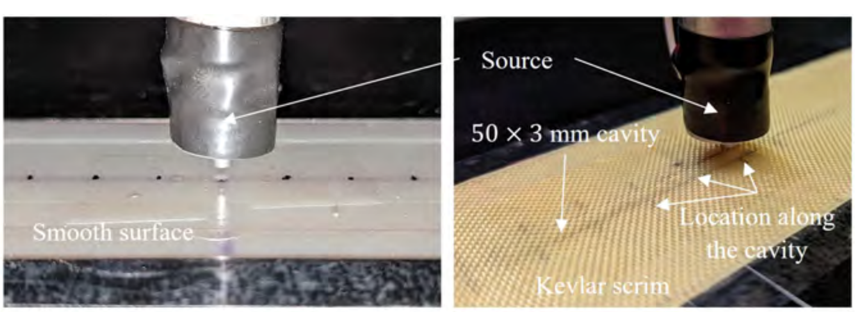

Fig. 5 Spatial sensitivity measurement setup: a) reference case without cavity; b) over the Kevlar-interfaced cavity showing the source and discrete source locations along the sensor.

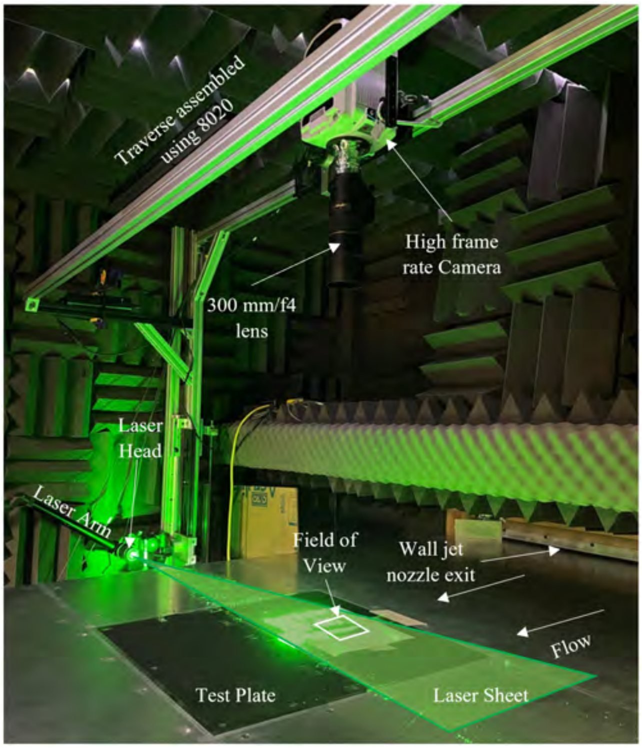

Fig. 6 Wall-parallel planar particle image velocimetry (PIV) setup in the wall jet facility.

The PIV setup comprised a Phantom v2512 high-speed camera (1280×800 pixels), a Photonics DM150-532 high-speed laser, and a LaVision high-speed controller, as shown in Fig. 6. Seeding was introduced into the flow at the suction side of the wind tunnel fan using an MDG MAX300APS fog generator. Employing a 300 mm/$f4$ Nikon lens at an aperture of f5.6 enabled detailed flow-field analysis. The distance between the front lens and the laser sheet was 1.2 m, yielding a field of view (FOV) size of 100×70 mm with a spatial resolution of 13.13 pixels/mm.

Image calibration utilized pinhole camera model calculations and a LaVision 106-10 calibration plate. The laser sheet thickness within the FOV was measured using a fine-scale ruler and found to be 1.5 mm. Flow images were processed using LaVision DaVis 10 software and an NVidia RTX2080 GPU for temporal correlation calculations. Multipass vector calculation involved initially using a larger 64×64 pixel window size with 50% overlap, followed by a smaller 16×16 pixel window with 75% overlap.

Two types of data were captured. First, data were acquired at a sampling rate of 10,240 frame pairs per second (FPS), providing two sets of 10,240 frame pairs, each corresponding to 1 s of flow time. Second, the sampling rate was 1024 FPS, obtaining 10,240 image pairs corresponding to 10 s of data. The former facilitated fine temporal flow analysis, while the latter enabled spatial flow analysis. In both cases, the dual frames of each image pair were spaced by 22 μs, resulting in a particle displacement of 7–8 pixels. A statistical convergence analysis of Reynolds stresses within the FOV indicated that 2 s of flow data provided a 98% convergence of mean Reynolds stresses.

III. Mathematical Model to Estimate Wall Pressure Spectrum

Assuming that the sensor averages over its surface (shown in Sec. IV.B), the measured pressure field by the sensor can be written as a convolution between the true pressure field over the sensor surface and its sensitivity function, which defines its averaging behavior as shown in Eq. (2).

$$q(\boldsymbol{x}, t) = \iint_{-\infty}^{\infty} A(\boldsymbol{s} - \boldsymbol{x}) p(\boldsymbol{s}, t) \mathrm{d}s_1 \mathrm{d}s_3 \tag{2}$$

Here, $p(\boldsymbol{s}, t)$ is the true pressure field over the surface of the sensor and $A(\boldsymbol{s} - \boldsymbol{x})$ represents the spatial sensitivity over all points $\boldsymbol{s}$ relative to a reference point $\boldsymbol{x}$ on the sensor surface. Note that the sensitivity function integrates to one and does not account for the cavity resonance response. Considering two sensors in space separated by $\Delta\boldsymbol{x} = \boldsymbol{x}' - \boldsymbol{x}$, the time delay correlation can be represented (with the same sensitivity function) as

$$R_{qq}(\boldsymbol{x}, \boldsymbol{x}', \tau) = E\big[q(\boldsymbol{x}, t), q(\boldsymbol{x}', t + \tau)\big]$$

$$R_{qq}(\boldsymbol{x}, \boldsymbol{x}', \tau) = \iint_{-\infty}^{\infty} \iint_{-\infty}^{\infty} A(\boldsymbol{s} - \boldsymbol{x}) A(\boldsymbol{s}' - \boldsymbol{x}') R_{pp}(\boldsymbol{x}, \boldsymbol{x}', \tau) \mathrm{d}s_1 \mathrm{d}s_3 \mathrm{d}s_1' \mathrm{d}s_3' \tag{3}$$

where m and n represent the two different sensors. For a homogeneous pressure field, R_{pp} can be expressed in terms of the wavenumber–frequency spectrum of surface pressure fluctuations, $\phi_{pp}(\boldsymbol{k}, \omega)$ as

$$R_{pp}(\Delta\boldsymbol{x}, \tau) = \iiint_{-\infty}^{\infty} \phi_{pp}(\boldsymbol{k}, \omega) e^{i\boldsymbol{k}.\Delta\boldsymbol{x}} e^{-i\omega t} \mathrm{d}k_1 \mathrm{d}k_3 \mathrm{d}\omega \tag{4}$$

where $\boldsymbol{k}$ is the wavenumber vector field that comprises of the streamwise wavenumbers k_1 and the spanwise wavenumbers k_3. Substituting Eq. (4) into Eq. (3) gives

$$R_{qq}(\Delta\boldsymbol{x}, \tau) = \iiint_{-\infty}^{\infty} \phi_{pp}(\boldsymbol{k}, \omega) e^{i\boldsymbol{k}.\Delta\boldsymbol{x}} e^{-i\omega t} \mathrm{d}k_1 \mathrm{d}k_3 \mathrm{d}\omega \times \iint_{-\infty}^{\infty} A(\boldsymbol{s} - \boldsymbol{x}) \mathrm{d}s_1 \mathrm{d}s_3 \iint_{-\infty}^{\infty} A(\boldsymbol{s}' - \boldsymbol{x}') \mathrm{d}s_1' \mathrm{d}s_3' \tag{5}$$

Distributing the exponential inverse Fourier term to the sensitivity functions and considering the Fourier transform of the spatial sensitivity function $A(\boldsymbol{s} - \boldsymbol{x})$ for a sensor,

$$A(\boldsymbol{k}, \boldsymbol{x}) = \frac{1}{4\pi^2} \iint_{-\infty}^{\infty} A(\boldsymbol{s} - \boldsymbol{x}) e^{-i\boldsymbol{k}.\boldsymbol{s}} \mathrm{d}s_1 \mathrm{d}s_3 \tag{6}$$

Substituting for $\boldsymbol{s} - \boldsymbol{x}$ as $\boldsymbol{z}$ and noting the independence of the sensitivity function to the sensor location $\boldsymbol{x}$, the above equation reduces to

$$A(\boldsymbol{k}, \boldsymbol{x}) = \frac{1}{4\pi^2} \iint_{-\infty}^{\infty} A(\boldsymbol{z}) e^{-i\boldsymbol{k}.(\boldsymbol{x}+\boldsymbol{z})} \mathrm{d}z_1 \mathrm{d}z_3 = \frac{e^{-i\boldsymbol{k}.\boldsymbol{x}}}{4\pi^2} \iint_{-\infty}^{\infty} A(\boldsymbol{z}) e^{-i\boldsymbol{k}.\boldsymbol{z}} \mathrm{d}z_1 \mathrm{d}z_3 = A(\boldsymbol{k}) e^{-i\boldsymbol{k}.\boldsymbol{x}} \tag{7}$$

At the center of the sensor, $\boldsymbol{x} = 0$, giving $A(\boldsymbol{k}, \boldsymbol{x} = 0) = A(\boldsymbol{k})$. Consider two sensors m and n positioned at (x_m, x_n) with $x_m - x_n = \Delta x$, and Eq. (5) can then be written as

$$R_{qq}(\boldsymbol{x}_m, \boldsymbol{x}_n, \tau) = \iiint_{-\infty}^{\infty} \phi_{pp}(\boldsymbol{k}, \omega) e^{-i\omega t} 4\pi^2 A_m(\boldsymbol{k}) e^{-i\boldsymbol{k}.\boldsymbol{x}_m} 4\pi^2 A_n^*(\boldsymbol{k}) e^{i\boldsymbol{k}.\boldsymbol{x}_n} \mathrm{d}k_1 \mathrm{d}k_3 \mathrm{d}\omega$$

$$R_{qq}(\Delta\boldsymbol{x}, \tau) = 16\pi^4 \iiint_{-\infty}^{\infty} \phi_{pp}(\boldsymbol{k}, \omega) A_m(\boldsymbol{k}) A_n^*(\boldsymbol{k}) e^{i\boldsymbol{k}.(\boldsymbol{x}_n - \boldsymbol{x}_m)} e^{-i\omega t} \mathrm{d}k_1 \mathrm{d}k_3 \mathrm{d}\omega \tag{8}$$

Hence, the autospectrum of a single sensor ($\Delta\boldsymbol{x} = 0$) is obtained by taking the Fourier transform of the above equation and $A_m(\boldsymbol{k}) = A_n(\boldsymbol{k})$:

$$G_{qq}(\omega) = 16\pi^4 \iint_{-\infty}^{\infty} \phi_{pp}(\boldsymbol{k},\omega)|A(\boldsymbol{k})|^2 \mathrm{d}k_1 \mathrm{d}k_3 \tag{9}$$

where the term $\phi_{pp}(\boldsymbol{k},\omega)$ is the true pressure spectrum of the wall pressure under a homogeneous turbulent boundary layer. There exist models that can be used for this purpose such as described by Chase [9], Corcos [10], and Hwang et al. [11]. The analysis shown here will use the Chase model due to its semi-analytical nature. The wavenumber–frequency spectrum for the model is given by

$$\phi_{pp}(k_1,k_3,\omega) = \frac{\rho_0^2 u_\tau^3}{[\kappa_+^2 + (b\delta)^{-2}]^{5/2}} \left\{ \left(c_2 \frac{|K_c|^2}{\kappa^2} + c_3 \frac{\kappa^2}{|K_c|^2} + 1 - c_2 - c_3 \right) \times C_T \kappa^2 \frac{[\kappa_+^2 + (b\delta)^{-2}]}{[\kappa^2 + (b\delta)^{-2}]} + C_M \frac{\kappa^2}{|K_c|^2} k_1^2 \right\} \tag{10}$$

where the terms are defined as

$$\kappa^2 = k_1^2 + k_3^2$$
$$\kappa_+^2 = \kappa^2 + \left[\left(\frac{\omega}{U_c} - k_1 \right) \frac{U_c}{hu_\tau} \right]^2$$
$$\kappa_c^2 = \left(\frac{\omega}{c_\infty} \right)^2 - \kappa^2 \tag{11}$$

and the constants are $C_T = 0.014/h$, $h = 3$, $C_M = 0.466/h$, $b = 0.75$, and $c_2 = 1/6 = c_3$. It is important to note that this estimate does not account for the cavity response function that forms part of the calibration function of the sensor. The validity of this estimated model is shown in Sec. IV.D, highlighting the features captured and the discrepancies.

IV. Results and Discussion

In Sec. IV.A, we showcase measurements illustrating the dynamic correlation between a uniform pressure experienced atop a Kevlar-covered cavity and the signal recorded by a microphone positioned at the bottom of the sensor. We analyze the dynamic response of sensor types A through E in Table 1 to ascertain the coherence of the pressure field within a quarter-wave cavity and to observe the impact of profile shape. Section IV.B presents measurements of pressure field coherence at the base of sensors B and E, which are crucial for this sensor behavior. Additionally, the section discusses precise measurements conducted using the highly localized monopole source traversing over the top of sensor type D. These measurements aim to establish spatial sensitivity functions associated with these Kevlar-covered sensors. Section IV.C focuses on quantifying the effects of a Kevlar-covered cavity on turbulent wall-jet boundary-layer flow, employing a half-wave cavity. A special section is included toward the end, which identifies challenges with these types of sensors, still rendering them useful for acoustic measurements under flow but not for wall pressure measurements.

A. Sensor Dynamic Response

Figure 7 illustrates the dynamic response for all sensors in Table 1 except F and J. Sensors B through E were covered with a Kevlar 120 scrim (0.08 mm thick, with a thread density of 34 filaments per inch in both directions and 2% OAR). Sensor A serves as the reference in this set, featuring a slot profile and lacking a Kevlar interface. The dynamic response function of each configuration is depicted in Fig. 7, presented in 1/12th octave bins. The blue curve represents the slot, the red depicts a rectangle, and the green signifies the mirrored Hanning profile; all spanning a length of 18 mm, a width of 3 mm, and a depth of 21 mm. Sensor D has a rectangular profile with a length of 50 mm but maintains the same width and depth as the others. The low-frequency variation falls within the uncertainty limits of ± 0.8 dB. The resonant depth mode of the reference sensor A is observed to be approximately at 3.6 kHz (first peak), which closely aligns with the theoretical quarter-wave mode of 4 kHz. However, Kevlar-covered

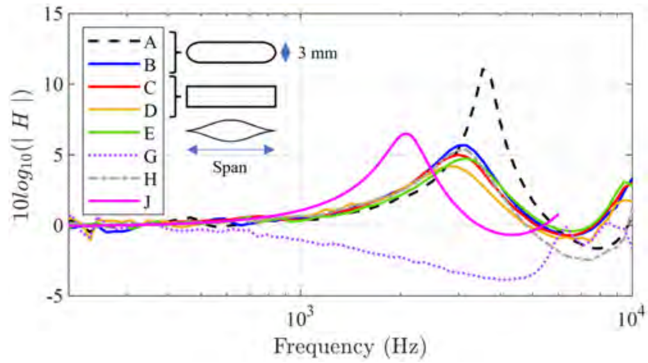

Fig. 7 Sensor dynamic response showcasing effects of profile shapes and Kevlar porosity.

sensors exhibit a drop in the modal frequency response to about 3 kHz for the first mode. This is attributed to a change in the impedance boundary condition due to the Kevlar scrim and end effects. The sensor dynamic response function demonstrates a notable similarity across various Kevlar-interfaced shapes tested, indicating consistent depth resonance characteristics. However, concluding the impact of profile shape on sensor dynamic response without considering the pressure field at the base of the cavity would be misleading. The figure also shows the dynamic response of sensors G and H using a different OAR Kevlar scrim. Sensor G experiences damping between 1 and 5 kHz due to a near-closed boundary condition (OAR = 0.01%) or potentially to a cavity-membrane-type resonator system. This can only be known on further characterization, which is beyond the scope this work. Sensor H has a similar second-order response to the 2% OAR Kevlar case (sensor B). The change in OAR does not appear to affect sensor H at its resonance mode, but a drop at higher frequencies suggests a shift in the impedance boundary. Sensor J's response is shown in magenta and is similar in form to other cases; however, it differs in resonance due to a higher cavity depth. It is also cut off at 6 kHz due to an acoustic source limitation used for calibrating this sensor [7].

B. Spatial Sensitivity

The coherence between the two microphones at the base of two sensors (B and E) is shown as a contour map in Fig. 8. The abscissa shows the location along the cavity base, and the ordinate shows the frequency in kilohertz on a logarithmic scale. The choice of coherence was made due to a consistent behavior observed in the pressure ratio between the two microphones. The coherence for sensor type B (Fig. 8) shows a near-unity value until about 10 kHz, which is the resonant mode of the volumetric cavity along its length (referred to as the cross-mode). Beyond this frequency, a drop in coherence is observed as one moves away from the center of the cavity. The coherence maps are supported with a corresponding phase map showing the unwrapped phase between the two microphones. The behavior here is consistent with that of the coherence maps. Figure 8 shows the results for sensor type E with a Hanning profile. The behavior is very similar to sensor type B except with some changes in the resonant mode (≈14 kHz). This is expected due to edge effects from the converging ends of the profile.

Figure 9 displays a schematic depicting source locations and the sensor dynamic response of the sensor. The sensor dynamic response has been normalized based on spatially averaged pressure amplitude, assuming an ideal monopole source positioned over a rectangular surface. The sound field generated by the source was validated against a pressure field measurement performed indirectly using a traversing speaker over a fixed probe microphone. This monopole field was represented using a volumetric source equation, employing the same source locations over the cavity as experimentally tested. A two-dimensional domain, slightly larger than the cavity dimensions, was selected, and the averaged pressure amplitude over the cavity region was calculated. The residual between the average pressure amplitude when the source is positioned at the center of the cavity and

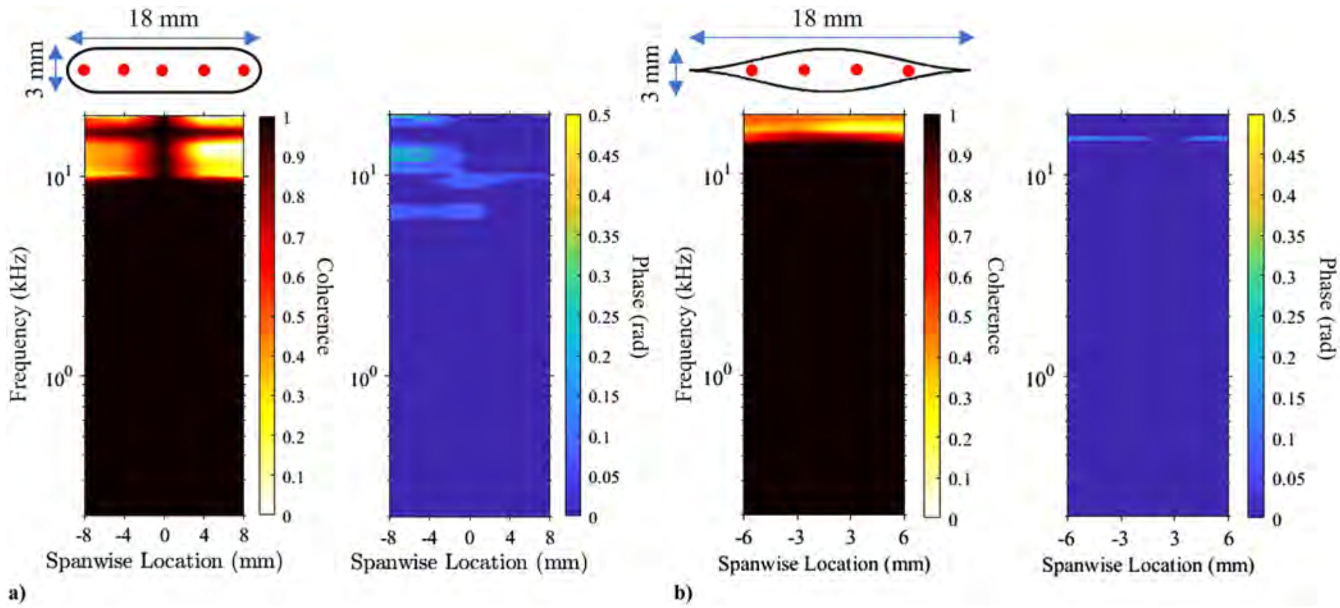

Fig. 8 Spanwise coherence and phase contour for a) sensor *B* and b) sensor *E* when excited using turbulent flow. The location of the traversing microphone is shown with respect to the sensor profile.

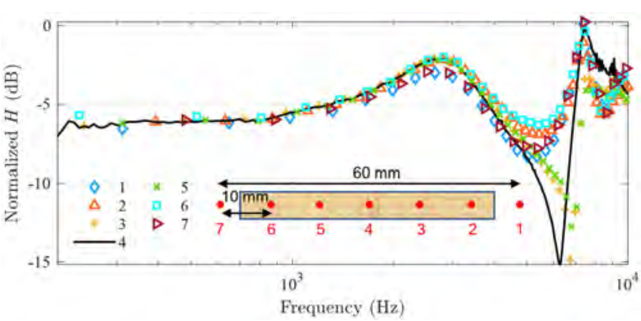

Fig. 9 Sensor dynamic response for sensor type *D* when excited using a localized monopole source along its surface as depicted.

when it occupies other locations was calculated and then subtracted from the measured data. Notably, the plots converge as the disparity in spatially averaged levels is addressed through residual subtraction. It is important to note that the microphone was fixed at the bottom center of the cavity for all measurements, with only the source location varied. The response functions' behavior remains within an uncertainty band of ± 0.8 dB for all source locations until reaching a frequency of approximately 3.4 kHz, beyond which deviations occur. This frequency is associated with a resonant mode along the span of the cavity (cross-mode) that breaks the uniform pressure field. Source locations equidistant from the center of the cavity exhibit a similar trend, consistent with the symmetric nature of the sound field. The first peak corresponds to the resonant mode of the cavity, which is lower than the theoretical mode due to the presence of a Kevlar interface.

These findings demonstrate that the Kevlar-interfaced cavity can be approximated with a constant spatial sensitivity, effectively averaging pressure across its surface. It is important to note that this capability of the Kevlar-covered sensor is based on a handful of measurement points, and the true behavior is affected at the edges of the cavity. The true behavior will be a function of Kevlar attachment and the cavity.

C. Flow Disturbance Quantification

Two regimes characterize a wall jet flow over a flat plate: lower and upper. The lower regime resembles a turbulent boundary-layer flow until a maximum is reached in the velocity profile (U_m), while the upper portion comprises a two-dimensional planar shear layer that extends to the quiescent air. The boundary layer is defined by a thickness of 13.3 mm over the sensor location, where the measurements were obtained and the maximum velocity magnitude was $U_m = 24$ m/s. The friction Reynolds number Re_τ was found to be 990 using curve fits on the velocity profile to find the wall shear stress. The mean flow behavior from the PIV was found to agree with previous studies performed in the same facility (Szőke et al. [12]) and the nature of a wall jet boundary layer. It is to be noted that the viscous unit (ν/u_τ) was measured as 0.0134 mm.

Regarding flow disturbance, we can anticipate several effects from the cavity on the flow dynamics. Firstly, there may be a standing wave within the cavity, which could act as an excitation to the flow. An examination of the wavenumber–frequency spectrum of the flow passing over the cavity could assess this effect. Since the flow is homogeneous in both the streamwise and spanwise directions, obtaining this quantity is relatively straightforward and is discussed further in subsequent paragraphs. In the scenario where a constant pressure difference exists over the two sides of the cavity (i.e., below and above), a bias flow may develop across the cavity. However, this concern can be disregarded in this context due to the parallel streamlines above the plate, the previously observed zero-pressure gradient in the wall jet, and the fact that the air volume beneath the cavity matches that in the wall jet flow. Lastly, there might be an interaction between the Kevlar material and the flow. Although direct measurement of this effect is not yet available in the literature, indirect evidence suggests that Kevlar behaves as an approximation to a no-slip wall when no pressure difference is present on the two sides of the fabric (Szőke et al. [13,14]). This behavior has been observed in previous studies and holds in this case.

The no-slip behavior of Kevlar fabric can be attributed to two of its properties: the OAR and the pore size within the fabric. The OAR for the Kevlar used here is 2% (Szőke et al. [13]), and the weave density, measured as threads per inch (TPI), is 34 in both the warp and weft directions. Calculations based on these properties reveal a pore size of approximately 0.1 mm, equivalent to 7.5 viscous units. The small OAR effectively suppresses any bias flow from passing through the fabric, while the fine distribution of pores and their small size reduce the likelihood of flow interactions. From the flow's perspective, Kevlar is perceived as a 98% solid wall.

Figure 10 depicts maps illustrating the mean flow characteristics over the Kevlar-interfaced cavity, measured at 1.25 mm parallel to the wall. The horizontal axis represents the distance along the flow direction, while the vertical axis denotes the spanwise direction. The streamwise mean velocity remains relatively constant at approximately

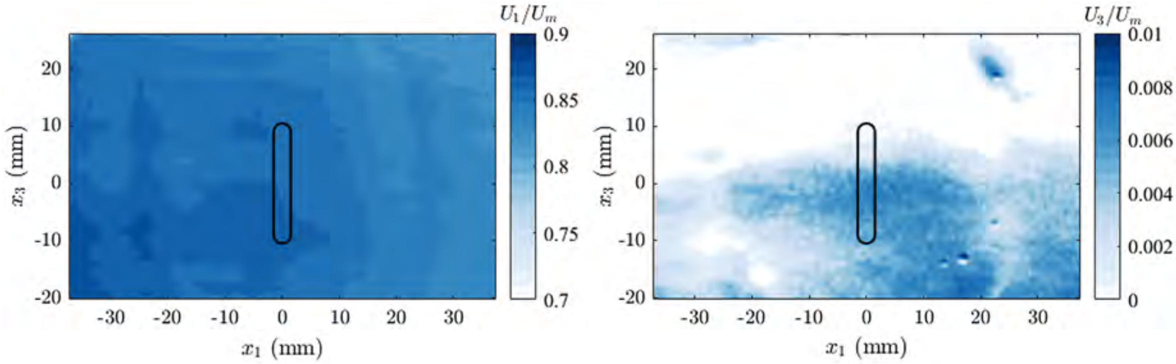

Fig. 10 Mean flow statistics in a wall-parallel plane over the Kevlar-interfaced cavity surface. The black outline shows the location of the sensor underneath. *Left:* normalized streamwise component; *right:* spanwise component.

$0.85U_m \pm 0.07U_m$, exhibiting no discernible variation across the cavity, as evident from the values displayed. Additionally, the spanwise mean flow, illustrated in Fig. 10 (right), is minimal, accounting for less than 1% of U_m, further indicating the negligible impact of the cavity on the mean flow.

Furthermore, turbulence statistics, depicted in Fig. 11, reveal consistent levels of streamwise turbulent normal stress (Fig. 11 (left)) and spanwise turbulent normal stress (Fig. 11 (right)), averaging at approximately $0.16U_m \pm 0.004U_m$ and $0.15U_m \pm 0.006U_m$, respectively. This uniformity suggests that the cavity has little influence on turbulence statistics.

Figure 12 (left) presents the autospectrum of streamwise velocity fluctuations at the streamwise location of the cavity centerline ($x_1 = 0$), plotted against frequency and spanwise position (x_3). The normalized autospectral density shows a collapse (within 0.8 dB) among the three locations, indicating a spanwise uniformity. Though not displayed here, this uniformity is generally observed at all streamwise positions upstream and downstream of the cavity. To further evaluate any potential effect of the cavity on turbulence spectral structure, Fig. 12 (right) illustrates the line spectrum at the centerspan ($x_3 = 0$) at three streamwise locations: the center of the cavity ($x_1 = 0$), upstream of the cavity ($x_1 = -30$), and downstream of the cavity ($x_1 = 30$). The resonant frequency of the cavity corresponds to an $f\delta/U_m = 1.66$, which does not show any relevant discrepancies in the spectra. Moreover, the spectra at all stations exhibit consistency within 2 dB, indicating that the cavity does not significantly interfere at the presented timescales.

The resonator cavity may extract energy weakly from the flow at spanwise modes consistent with the cavity span. To explore this possibility, we utilized measurements to estimate the frequency–wavenumber spectrum $G_{uu}(f, k_3)$, which breaks down the autospectrum displayed in Fig. 12 (right) based on wavenumber. Figure 13 depicts the frequency–wavenumber spectrum, $G_{uu}(f, k_3)$, upstream, at the center, and downstream of the cavity, respectively, corresponding to the x_1 locations of each line spectrum in Fig. 12 (right). The color scale shows $10\log_{10}(G_{uu}/U_m\delta^2)$, x axis shows the normalized frequency, and the y axis shows the normalized spanwise wavenumber. Contours of the wavenumber spectra, normalized with

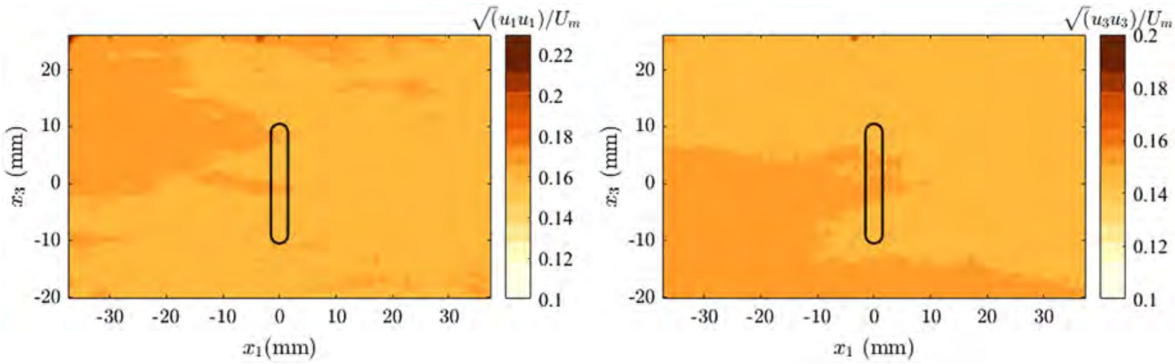

Fig. 11 Turbulence statistics in a wall-parallel plane over the Kevlar-interfaced cavity surface. The black outline shows the location of the sensor underneath. *Left:* normalized streamwise component; *right:* spanwise component.

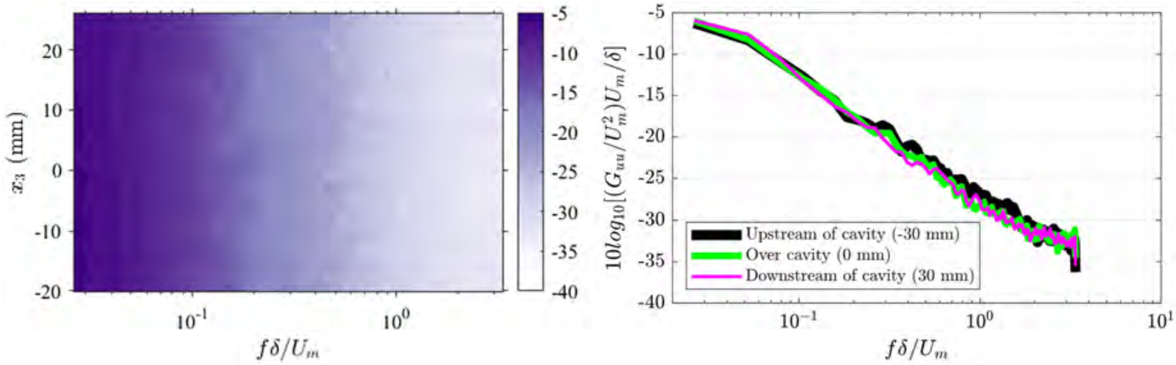

Fig. 12 Normalized streamwise velocity spectrum. *Left:* over sensor center line; *right:* at three streamwise points.

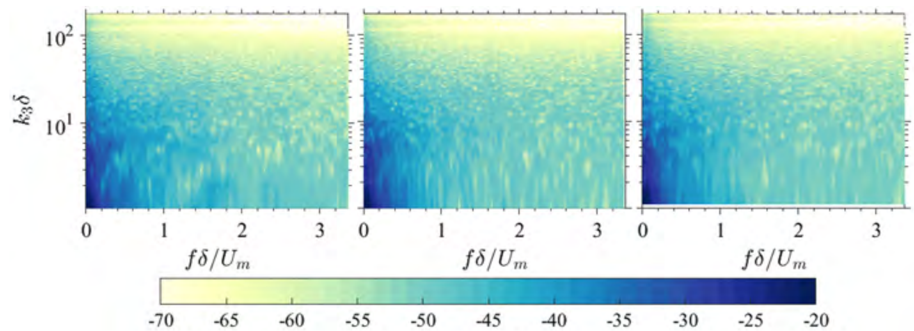

Fig. 13 Spanwise wavenumber–frequency spectrum at three streamwise locations. *Left:* upstream of cavity ($x = -30$ mm); *middle:* center of cavity ($x = 0$ mm); *right:* downstream of cavity ($x = 30$ mm).

boundary-layer length and time scales (δ, U_m), suggest that the cavity's influence on the flow, even at modes matching the cavity span ($k_3\delta = 4.65$), remains within the bounds of uncertainty.

In a study by Damani [15], examination of the mean flow, Reynolds stresses, and turbulence spectrum in the wall-normal cross section revealed minimal impact of the Kevlar-interfaced cavity on the flow in a plane aligned with the wall's direction and passing through a half-wave cavity, part of an acoustic metasurface. Comparison of streamwise and wall-normal velocity indicated differences between the cavity and baseline cases within measurement uncertainty. While this suggests limited effect in a wall-normal cross section, any effect, if present, would likely be observable in a plane parallel to the cavity surface. It is conceivable that some turbulent energy is redirected toward exciting the Kevlar-interfaced cavity, particularly around the resonant frequency. This could lead to a reduction in the energy spectrum near wavenumbers corresponding to the cavity size. Alternatively, acoustic motions within the cavity might exert feedback on the flow.

D. Suitability for Wall Pressure Measurements

These observations, along with those from preceding sections, strongly indicate that the Kevlar-interfaced cavity serves as an area-averaging sensor that does not significantly influence the overlying flow, affirming its suitability for flow-sensing applications such as low-wavenumber pressure fluctuations and far-field noise detection through boundary layers. Low-wavenumber pressure measurements on turbulent boundary layers have been performed by arranging an array of Kevlar-interfaced cavities to filter out strong convective portions of turbulence while adequately resolving weaker subconvective portions, as demonstrated by Damani et al. [7].

While the measurements show uniform sensitivity over the central portions of the Kevlar membrane, it is unlikely that this uniformity is sustained up to the edges and corners of the membrane, since pressure will be transmitted into the cavity through the pores and the elastic deformation of the membrane. For this reason, the Kevlar covering may not be ideal when fine geometric details of the cavity shape are important, as can be the case in some subconvective pressure array designs. In other situations, however, such as measuring acoustics through the turbulent boundary layer where the key idea is to filter out the convective pressure fluctuations, this may be of no consequence.

This was demonstrated using measurements taken by Damani et al. [7] underneath a zero-pressure gradient boundary-layer flow. This case has been represented as configuration J in Table 1. Here, a Kevlar-covered sensor 50 mm in length, 3 mm in width, and 30 mm in depth was excited using a turbulent boundary layer ($\delta = 54.2$ mm, $\delta^* = 7.8$ mm, $U_\infty = 22.37$ ms^{-1}, $\theta = 5.9$ mm, $Re_\tau = 2860$, $Re_\theta = 8420$). Note that the sensor length was aligned with the flow as shown above the legend box in Fig. 14. The black curve in Fig. 14 shows the autospectral density in decibels as a function of frequency as measured by the sensor. The curve was obtained by dividing out the sensor acoustic calibration (curve J in Fig. 7) from the raw spectrum (green) to account for the cavity resonance of the system. Note that this assumes negligible effects of the evanescent subsonic pressure fluctuations, which are validated by the general agreement

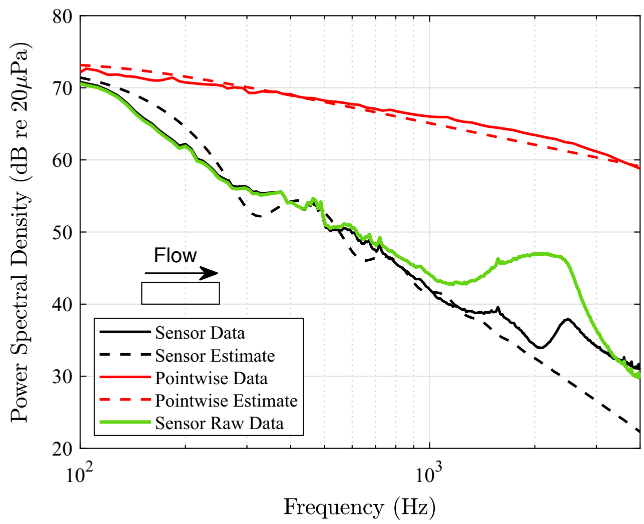

Fig. 14 Autospectral density of sensor J as compared to a pointwise wall pressure measurement. Solid: measured data; dash: model estimates.

(within 1.5 dB) observed between the flow data (solid) and the estimate from the model (dashed) until 2 kHz.

For reference, the measured pointwise spectrum is also plotted. The model estimates were evaluated using the compressible Chase model for a pointwise spectrum (red) and the sensor estimate from Eq. (9) in black. The sensor estimate assumes a uniform sensitivity function (rectangular window function) over the sensor that yields a behavior that slightly differs from the measurement but has an overall profile that agrees very well. There is a drop in level with increasing frequency due to the filtering of small-scale turbulence by the large sensor area. The model depicts side-lobe behavior, which arises due to the uniform sensitivity assumption, while, practically, this is not seen in the measurements, indicating a different sensitivity. The sensitivity profile is expected to have a form with tapering sensitivity toward the edges of the sensor; however, it is difficult to quantify without more data. The measurements also reveal some peaks and bumps beyond 1000 Hz, which are an artifact of change in the impedance of the system due to grazing flow effects. This is similar to grazing flow effects observed on pinhole microphone response as seen in the work of Fritsch et al. [16]. The dip observed at 2 kHz occurs due to the accounting of resonance of the cavity obtained from its calibration function. However, this does not completely account for the resonance of the system under grazing flow. The shift in resonance requires further investigation and is beyond the scope of this work.

From the wall pressure measurement results, it is clear that such Kevlar-covered sensors can filter medium- and high-wavenumber wall pressure components contributed by convective turbulence and have applications in shielding microphones from turbulent boundary-layer noise. Damani et al. [7] used this sensor concept with larger cavities to measure subconvective wall pressure spectrum, and the results suffered from aliasing effects. Attempts were made to extend this concept to sensors that selectively filter in space to minimize aliasing. This required a well-defined form of the sensitivity that was difficult to obtain for such sensors as their response had an inherent dependence on membrane effects (sensor type *G* in Fig. 7). Hence, the use of these sensors can be restricted to applications that are not sensitive to the true sensitivity of the sensors, such as turbulence noise shielding. Recently, this was tested by Galluscio et al. [17] with six Kevlar-covered sensors forming a beamforming array to detect source direction. The cavities had similar profiles as presented in this study, and the authors detected acoustic source direction. The array performance was comparable to the conventional array with six 1-inch microphones with an accuracy of 1°. However, the former used less-expensive, small-area microphones embedded in a Kevlar-covered cavity to improve performance. Hence, this array has advantages over conventional microphone arrays (with flush transducers) due to the use of cheaper microphones and flexibility in geometry from the cavity designs.

V. Conclusions

A new type of surface pressure sensor for measuring fluctuating pressures over large areas has been investigated. The convective pressure filtering ability and nonintrusive effects on the flow of Kevlar-covered, resonator-based cavity sensors establish their potential for use in flow applications such as detecting acoustic sources through turbulent boundary-layer flows or applications requiring shielding from high-frequency boundary-layer noise. These sensors are simple to construct in various forms using rapid prototyping technology and inexpensive transducers. The choice of transducer dictates the SNR of the system in addition to the depth of the cavity. Different sensor designs were tested to examine the influence of resonant cavity shape on the sensor's dynamic response and pressure field coherence. Additional tests were performed to quantify the spatial sensitivity function and evaluate the effects of a Kevlar flow interface on an overriding turbulent flow. A mathematical model to estimate the wall pressure spectrum using such sensors has been presented. The following conclusions were drawn:

1) The resonator-based cavity sensor offers flexibility in shape, with a dynamic response function that can be calibrated. The sensor's dynamic response is primarily limited by the physical dimensions of the cavity, particularly the fundamental mode associated with the largest dimension of the shape profile. The depth does not significantly impact the sensor's functional nature.

2) A Kevlar-covered acoustic resonator-based cavity exhibits area-averaging properties due to the large sensing area, making it viable as a pressure sensor for low- to midfrequency measurement applications.

3) A Kevlar-covered cavity has negligible effects on the flow, supporting the use of such systems in flow applications, especially in turbulent boundary-layer flows.

4) The thin flow interface over the resonator-based sensor acts as an impedance boundary condition, altering its dynamic response, which can be calibrated. The interface properties, including OAR, tune the dynamic properties of the resonating cavity system.

5) The mathematical model estimates seem to agree with data in an overall sense, assuming uniform spatial sensitivity; however, the discrepancies indicate the assumption to not be accurate.

Acknowledgments

The authors would like to thank the Office of Naval Research, in particular Dr. Greg Orris and Dr. Christine Sanders, for their support under grant N00014-21-1-2500. The authors at Exeter would like to thank Dr. John Smith and the Defence, Science, and Technology Laboratory for financially supporting this research.

References

[1] White, P. H., "Effect of Transducer Size, Shape, and Surface Sensitivity on the Measurement of Boundary-Layer Pressures," *Journal of the Acoustical Society of America*, Vol. 41, No. 5, 1967, pp. 1358–1363. https://doi.org/10.1121/1.1910482

[2] Kirby, G. J., "The Effect of Transducer Size, Shape and Orientation on the Resolution of Boundary Layer Pressure Fluctuations at a Rigid Wall," *Journal of Sound and Vibration*, Vol. 10, No. 3, 1969, pp. 361–368. https://doi.org/10.1016/0022-460X(69)90214-4

[3] Hu, N., "Sensor-Size-Related Attenuation Correction of Wall Pressure Spectra Measurements," *Physics of Fluids*, Vol. 34, No. 6, 2022, Paper 067119. https://doi.org/10.1063/5.0094847

[4] VanDercreek, C. P., Amiri-Simkooei, A., Snellen, M., and Ragni, D., "Experimental Design and Stochastic Modeling of Hydrodynamic Wave Propagation Within Cavities for Wind Tunnel Acoustic Measurements," *International Journal of Aeroacoustics*, Vol. 18, No. 8, 2019, pp. 752–779. https://doi.org/10.1177/1475472X19889949

[5] D'Elia, M. E., Humbert, T., and Aurégan, Y., "Effect of Flow on an Array of Helmholtz Resonators: Is Kevlar a "Magic Layer"?," *Journal of the Acoustical Society of America*, Vol. 148, No. 6, 2020, pp. 3392–3396. https://doi.org/10.1121/10.0002642

[6] Damani, S., Alexander, N., Devenport, W. J., Pearce, B. P., Shelley, S. R., Starkey, T. A., Hibbins, A. P., and Roy Sambles, J., "Excitation of Airborne Acoustic Surface Modes Driven by a Turbulent Flow," *AIAA Journal*, Vol. 59, No. 12, 2021, pp. 5011–5019. https://doi.org/10.2514/1.J060662

[7] Damani, S., Butt, H., Banks, J., Srivastava, S., Lowe, T. K., and Devenport, W. J., "Low-Wavenumber Wall Pressure Measurements in Zero-Pressure Gradient Boundary Layer Flow," *AIAA SciTech 2022 Forum*, AIAA Paper 2022-1795, 2022. https://doi.org/10.2514/6.2022-1795

[8] Kleinfelter, A. W., Repasky, R., Hari, N., Letica, S., Vishwanathan, V., Organski, L., Schwaner, J., Alexander, W. N., and Devenport, W. J., "Development and Calibration of a New Anechoic Wall Jet Wind Tunnel," *AIAA SciTech 2019 Forum*, AIAA Paper 2019-1936, 2019. https://doi.org/10.2514/6.2019-1936

[9] Chase, D., "The Character of the Turbulent Wall Pressure Spectrum at Subconvective Wavenumbers and a Suggested Comprehensive Model," *Journal of Sound and Vibration*, Vol. 112, No. 1, 1987, pp. 125–147. https://doi.org/10.1016/S0022-460X(87)80098-6

[10] Corcos, G., "The Resolution of Turbulent Pressures at the Wall of a Boundary Layer," *Journal of Sound and Vibration*, Vol. 6, No. 1, 1967, pp. 59–70. https://doi.org/10.1016/0022-460X(67)90158-7

[11] Hwang, Y. F., Bonness, W. K., and Hambric, S. A., "On Modeling Structural Excitations by Low Speed Turbulent Boundary Layer Flows, Techn. Rept. 03-008, 2003, 32, https://api.semanticscholar.org/CorpusID:118585377.

[12] Szőke, M., Hari, N. N., Devenport, W. J., Glegg, S. A., and Teschner, T.-R., "Flow Field Analysis Around Pressure Shielding Structures," *AIAA Aviation 2021 Forum*, AIAA Paper 2021-2293, 2021. https://doi.org/10.2514/6.2021-2293

[13] Szőke, M., Glegg, S. A., and Devenport, W. J., "Investigating the Aeroacoustic Properties of Kevlar Fabrics," *AIAA AVIATION 2021 FORUM*, AIAA Paper 2021-2255, 2021. https://doi.org/10.2514/6.2021-2255

[14] Szőke, M., Borgoltz, A., and Devenport, W. J., " Fluid–Structure Interaction Modeling of Flowfields Within Kevlar-Walled Wind Tunnels," *Journal of Aircraft*, Vol. 59, No. 5, 2022, pp. 1–14. https://doi.org/10.2514/1.C036724

[15] Damani, S., "Excitation of Acoustic Surface Waves by Turbulence," Virginia Tech. 2021, http://hdl.handle.net/10919/104742.

[16] Fritsch, D., Vishwanathan, V., Lowe, T., and Devenport, W. J., "The Effect of Grazing Flow on Pinhole Condenser Microphones," *AIAA Scitech 2021 Forum*, AIAA Paper 2021-0130, 2021. https://doi.org/10.2514/6.2021-0130 https://arc.aiaa.org/doi/abs/10.2514/6.2021-0130.

[17] Galluscio, C. A., Damani, S., Alexander, W. N., Devenport, W. J., and Starkey, T. A., "Wind Tunnel Testing of Directionally Sensitive Meander Metasurface and Sub-Resonant Sensor Arrays," *30th AIAA/CEAS Aeroacoustics Conference*, AIAA Paper 2024-3025, 2024. https://doi.org/10.2514/6.2024-3025

L. Ukeiley
Associate Editor